

## *Supporting Information*

### **Neglected but Efficient Electron Utilization Driven by Biochar Co-Activated Phenols and Peroxydisulfate: Polyphenol Accumulation Rather Than Mineralization**

Jibo Dou<sup>a</sup>, Yao Tang<sup>a</sup>, Zhijiang Lu<sup>c</sup>, Guangzhi He<sup>d</sup>, Jianming Xu<sup>a</sup>, Yan He<sup>a,b,\*</sup>

<sup>a</sup> *Zhejiang Provincial Key Laboratory of Agricultural Resources and Environment,  
Institute of Soil and Water Resources and Environmental Science, College of  
Environmental and Resource Sciences, Zhejiang University, Hangzhou 310058, China*

<sup>b</sup> *Key Laboratory of Environment Remediation and Ecological Health, Ministry of  
Education, Hangzhou 310058, China*

<sup>c</sup> *Department of Environmental Science and Geology, Wayne State University, Detroit,  
MI 48201, United States*

<sup>d</sup> *State Key Joint Laboratory of Environment Simulation and Pollution Control,  
Research Center for Eco-Environmental Sciences, Chinese Academy of Sciences,  
Beijing 100085, China*

*\*Corresponding author: Yan He; E-mail: yhe2006@zju.edu.cn; Tel.: +86-571-8898-  
2065; Fax: +86-571-8898-2065*

*This Supplementary Information includes*

**48 Pages, 16 Texts, 9 Tables, 18 Figures**

# Contents

<b>Part S1. Supplementary Texts</b>	4
Text S1. Chemicals.	4
Text S2. Preparation of rBC400 and oBC400.	4
Text S3. Characterizations of biochars.	5
Text S4. TCP-spiked soil experiments.	5
Text S5. Competitive kinetics experiments.	6
Text S6. Degradation product identification.	8
Text S7. Spectrophotometric determination of PDS.	9
Text S8. Fluorescence labeling of C=O groups.	9
Text S9. Boehm titration.	10
Text S10. EPR measurements.	10
Text S11. Singlet Oxygen Sensor Green method.	11
Text S12. The examination of $O_2^{\cdot-}$ by nitro blue tetrazolium.	11
Text S13. Analysis of <i>in situ</i> Raman.	12
Text S14. Two-chamber galvanic oxidation reactor.	12
Text S15. Electrochemical tests.	12
Text S16. Biochar molecular modeling and DFT calculations.	14
<b>Part S2. Supplementary Tables</b>	17
Table S1. Summary of the chronopotentiometry data according to the literature.	17
Table S2. The electron-equivalent data calculated according to the literature and this study.	18
Table S3. Detection parameters of HPLC.	19
Table S4. Observed degradation rate constants $k_{obs}$ of phenolic compounds.	20
Table S5. Open circuit potential (OCP) data of the three biochars.	21
Table S6. Second-order rate constants ( $M^{-1} s^{-1}$ ) between ROS and probe compounds.	21
Table S7. Quantitative analysis of O species in the biochars based on O 1s XPS spectra.	22
Table S8. Elemental compositions of different biochars as well as their PFR properties (i.e., g-factor), C=O, and phenolic –OH contents.	24
Table S9. Verification of the simulated biochar models.	25
<b>Part S3. Supplementary Figures</b>	26
Figure S1. (a) TCP removal by PDS oxidation and biochars adsorption, respectively. (b) Nitrogen adsorption-desorption isotherms (filled and open symbols correspond to the adsorption and desorption branches, respectively). (c) Normalized degradation rate constants by the specific surface area. Time profiles of TCP removal at pH = 7 and 10 (d and e) in the biochar/PDS systems. (f) The zeta potential-pH curves for the biochars produced at different pyrolysis temperatures. (Reaction conditions: $[PDS]_0 = 5 \text{ mM}$ , $[biochar] = 0.2 \text{ g L}^{-1}$ , $25 \text{ }^{\circ}\text{C}$ .)	26

62	<b>Figure S2.</b> Degradation profiles of various phenols in the biochar/PDS system. (Reaction	
63	conditions: $[PDS]_0 = 5 \text{ mM}$ , $[\text{biochar}] = 0.2 \text{ g L}^{-1}$ , $[\text{phenols}]_0 = 5 \text{ mg L}^{-1}$ , $25 \text{ }^\circ\text{C}$ .).....	27
64	<b>Figure S3.</b> (a) EPR spectra for the BC400 and BC500 activated PDS systems in water/tert-	
65	butyl alcohol ( $v/v = 1$ ). (b) EPR signals of TEMP adducts. (c) DMPO-trapped EPR	
66	spectroscopy analysis using MeOH as a solvent, and (d) UV-vis spectra for the examination of	
67	NBT <sup>2+</sup> . (Reaction conditions: $[PDS]_0 = 5 \text{ mM}$ , $[\text{biochar}] = 0.2 \text{ g L}^{-1}$ , $[\text{TCP}]_0 = 5 \text{ mg L}^{-1}$ , $[\text{DMPO}]$	
68	$= 25 \text{ mM}$ , $[\text{NBT}] = 0.01 \text{ mM}$ , $25 \text{ }^\circ\text{C}$ .).....	28
69	<b>Figure S4.</b> Quenching effects of different scavengers. (Reaction conditions: $[PDS]_0 = 5 \text{ mM}$ ,	
70	$[\text{biochar}] = 0.2 \text{ g L}^{-1}$ , $[\text{TCP}]_0 = 5 \text{ mg L}^{-1}$ , $[\text{Tert-butyl alcohol, TBA}] = [\text{Methanol, MeOH}] = 0.5$	
71	$\text{M}$ , $[p\text{-benzoquinone, } p\text{-BQ}] = 10 \text{ mM}$ , $[L\text{-tryptophan, } L\text{-TRP}] = 10 \text{ mM}$ , $[\text{Dimethyl sulfoxide,}$	
72	$\text{DMSO}] = 10 \text{ mM}$ , $25 \text{ }^\circ\text{C}$ .) .....	29
73	<b>Figure S5.</b> <i>In situ</i> Raman spectra of BC400 and BC500 combined with PDS ( $[PDS]_0 = 20 \text{ mM}$ ,	
74	$[\text{biochar}] = 5 \text{ g L}^{-1}$ , solution pH without adjustment). .....	30
75	<b>Figure S6.</b> (a) Two-chamber galvanic oxidation reactor. (b) Current formation and (c) TCP	
76	degradation in the reactor ( $[PDS]_0 = 10 \text{ mM}$ , $[\text{TCP}]_0 = 20 \text{ mg L}^{-1}$ , $25 \text{ }^\circ\text{C}$ .) .....	30
77	<b>Figure S7.</b> Dynamic Tafel curves obtained using biochars-coated GCE as the working	
78	electrode. ....	31
79	<b>Figure S8.</b> Electrochemical impedance spectroscopy Nyquist plots. ....	32
80	<b>Figure S9.</b> Degradation of TCP, nitrobenzene (NB), and benzoic acid (BA) in different systems.	
81	(Reaction conditions: $[PDS]_0 = 5 \text{ mM}$ , $[\text{biochar}] = 0.2 \text{ g L}^{-1}$ , $[\text{TCP}]_0 = 5 \text{ mg L}^{-1}$ , $[\text{BA}]_0 = [\text{NB}]$	
82	$_0 = 0.01 \text{ mM}$ , $25 \text{ }^\circ\text{C}$ .).....	32
83	<b>Figure S10.</b> (a) Time course of furfuryl alcohol (FFA) removal. (b-d) Competitive degradation	
84	between TCP and 3-methoxy-phenol (MOP). (Reaction conditions: $[PDS]_0 = 5 \text{ mM}$ , $[\text{biochar}]$	
85	$= 0.2 \text{ g L}^{-1}$ , $[\text{TCP}]_0 = [\text{MOP}]_0 = 0.025 \text{ mM}$ , $[\text{FFA}]_0 = 2 \text{ mM}$ , $25 \text{ }^\circ\text{C}$ .) .....	33
86	<b>Figure S11.</b> (a) Concentration changes of PDS in biochar and thermal activation systems, and	
87	TCP degradation (dashed line) in thermal activation system. (Reaction conditions: $[PDS]_0 = 5$	
88	$\text{mM}$ , $[\text{biochar}] = 0.2 \text{ g L}^{-1}$ , $[\text{TCP}]_0 = 5 \text{ mg L}^{-1}$ , heating temperature = $70 \text{ }^\circ\text{C}$ .) (b) Photograph	
89	of the gelatinous substances in toluene after drying.....	34
90	<b>Figure S12.</b> (a) Structural formulas for the selected pollutants. (b) Photographs of degradation	
91	products dissolved in toluene. (c) Gel permeation chromatogram of the products eluted by	
92	toluene. (d, e) LC-MS spectrum of the products of aniline after ethanol elution. GC-MS	
93	chromatograms of the products in the (f-h) chlorobenzene/BC800/PDS and (i, j) 4-	
94	chlorobiphenyl/BC800/PDS systems. (Reaction conditions: $[PDS]_0 = 50 \text{ mM}$ , $[\text{biochar}] = 2 \text{ g}$	
95	$\text{L}^{-1}$ , $[\text{AN}]_0 = [\text{CB}] = [\text{CBP}] = 15 \text{ mM}$ .) .....	35
96	<b>Figure S13.</b> The reversible transformation of RAMs on biochars.....	36
97	<b>Figure S14.</b> Fitted curves of high-resolution XPS O1s spectrum of (a-e) fresh biochars and (f-	
98	j) used biochars after washing. (k) FTIR spectra and (l) PFRs intensity of biochars with tuned	

99	RAM compositions. (m) Degradation of benzoic acid (BA) in different systems. (Reaction	
100	conditions: $[PDS]_0 = 5 \text{ mM}$ , $[\text{biochar}] = 0.2 \text{ g L}^{-1}$ , $[\text{BA}]_0 = 0.01 \text{ mM}$ , $25 \text{ }^\circ\text{C}$ .) (n) Changes in	
101	the PFRs signals and (o) TCP removal efficiencies of BC500 before and after the reaction.	
102	(Reaction conditions: $[PDS]_0 = 5 \text{ mM}$ , $[\text{biochar}] = 0.2 \text{ g L}^{-1}$ , $[\text{TCP}]_0 = 5 \text{ mg L}^{-1}$ , $25 \text{ }^\circ\text{C}$ .) .....37	
103	<b>Figure S15.</b> The FTIR spectrum of biochars. ....41	
104	<b>Figure S16.</b> Optimized configurations of BC500, BC800, and $\text{S}_2\text{O}_8$ . (purple: C, white: H, red:	
105	O, yellow: S.) .....41	
106	<b>Figure S17.</b> Gaps between HOMO and LUMO of the biochar models.....42	
107	<b>Figure S18.</b> Schematic diagram of biochar properties and reactivity as a function of pyrolysis	
108	temperature. ....42	
109	<b>References</b> .....43	

## Part S1. Supplementary Texts

### Text S1. Chemicals.

Sodium persulfate, p-benzoquinone, 5,5-dimethyl-1-pyrroline N-oxide (DMPO), 2,2,6,6-tetramethyl-4-piperidinol (TEMP), benzoic acid, nitrobenzene, nitro blue tetrazolium, and 2,7-dichlorodihydrofluorescein diacetate ( $\text{H}_2\text{DCFDA}$ ) were purchased from Aladdin (Shanghai, China). Tert-butyl alcohol and furfuryl alcohol were obtained from Macklin (Shanghai, China). L-tryptophan, phenol, hydroquinone, 4-methylphenol, 4-chlorophenol, 4-nitrophenol, 4-hydroxybenzoic acid, 2,6-dimethylphenol, 3-methoxy-phenol, 2,6-dichlorophenol, and 2,4,6-TCP were supplied by Sigma-Aldrich (Shanghai, China). Singlet Oxygen Sensor Green was purchased from Meilunbio (Dalian, China). Ultrapure water with a resistivity of  $18.2 \text{ M}\Omega\cdot\text{cm}$  was used for all experiments.

### Text S2. Preparation of rBC400 and oBC400.

For rBC400 preparation, 5 g of BC400 was dispersed in 250 mL 5 wt %  $\text{NaBH}_4$  solution and then stirred continuously under anoxic conditions for 20 h at  $25 \text{ }^\circ\text{C}$ . After

that, the suspension pH was adjusted to about 7.0 by adding HCl solution, then stirred for another 4 h. The obtained mixture was filtered by a vacuum suction filter (0.45  $\mu\text{m}$ ), washed with deionized water thoroughly, and dried at 60  $^{\circ}\text{C}$ .

Additionally, 5 g of BC400 was added into 250 mL 5 wt %  $\text{H}_2\text{O}_2$  solution. Then, the mixture was stirred for 24 h at 60  $^{\circ}\text{C}$  in the air (without pH adjustment). Finally, the collected samples were washed, dried at 60  $^{\circ}\text{C}$ , and denoted as oBC400.

### **Text S3. Characterizations of biochars.**

Brunauer-Emmett-Teller (BET) specific surface areas of biochars were analyzed by a TriStar II analyzer at 77 K based on  $\text{N}_2$  adsorption/desorption methods. Fourier transform infrared spectroscopy (FTIR) spectra were performed on a NicoLET iS50 FTIR instrument (Thermo Scientific Co., Ltd., USA) in the wavenumber range of 500-4000  $\text{cm}^{-1}$ . Raman spectra were obtained on a Labram HR evolution spectrometer. The surface elemental compositions of biochars were recorded on X-ray photoelectron spectroscopy (XPS, ESCALAB 250Xi, Thermo Scientific Co., Ltd., USA) with an Al  $\text{K}\alpha$  X-ray source. The zeta potentials of biochars were analyzed using a Zetasizer Nano ZS90 Potential Analyzer (Malvern, UK). Ultimate analysis was performed using an elemental analyzer (Elementar vario EL, Germany) to determine the C, H, N, and S contents in the biochars. Solid-state  $^{13}\text{C}$  nuclear magnetic resonance (NMR) spectra were acquired with an Avance III HD 400 spectrometer operating at room temperature.

### **Text S4. TCP-spiked soil experiments.**

Soil for the experiments was collected from a non-polluted zone in Yingtan, Zhejiang Province at a depth of 0-20 cm, and passed through a 1 mm sieve before use. 1 kg of

soil was mixed with 20 mg TCP-acetone solution and stirred thoroughly, followed by the evaporation of acetone for 2 days under a fume hood. Finally, the spiked soil sample was aged for one month in the fume hood. The initial TCP concentration of the spiked soil sample was determined to be  $14.9 \text{ mg kg}^{-1}$ .

To study the oxidation efficiency of the BC/PDS system in soil, 25 g of spiked soil was transferred into a 100 mL brown vial, and the soil-water ratio was adjusted to 1:2. Subsequently,  $0.5 \text{ g L}^{-1}$  BC sample was homogenously mixed into the soil, and then  $1.5 \text{ g L}^{-1}$  PDS was added. Next, the flask was sealed with aluminum foil and placed on a magnetic stirrer at  $25^\circ\text{C}$ .

Periodically, 2 g of freeze-dried soil was sampled and extracted with 25 mL dichloromethane/n-hexane ( $V/V = 2$ ) in ultrasonic for 30min at  $35^\circ\text{C}$ . Transferring the extracts into a separatory funnel, and then the extract was added water (2 times the volume of the extract). Solution pH was adjusted to greater than 12 with NaOH, shaken sufficiently, discarded the lower organic phase, and retained the aqueous phase. The obtained aqueous phase was acidified with HCl until  $\text{pH} < 2$ . Subsequently, TCP was transferred to an organic phase by the addition of 50 mL dichloromethane/ethyl acetate ( $V/V = 4$ ), concentrated by a rotary evaporator and pressure-blowing concentrator, finally, the contents were resuspended in 2 mL methanol and transferred to a sample vial sample for HPLC analysis.

#### **Text S5. Competitive kinetics experiments.**

To further distinguish the relative contributions of  $\text{SO}_4^{\bullet-}$ ,  $^{\bullet}\text{OH}$ , and nonradical oxidation pathways for TCP degradation, the competitive kinetics experiment was

performed using the mixed system containing nitrobenzene (NB), benzoic acid (BA), and TCP. Prior to the competitive degradation experiment, the adsorption equilibrium of NB, BA, and TCP in the biochar suspension was achieved by pre-adsorption experiments. Based on the second-order rate constants (Table S6), the steady-state concentrations of  $\cdot\text{OH}$  were calculated using NB, because NB primarily reacts with  $\cdot\text{OH}$ , while the reaction with  $\text{SO}_4^{\cdot-}$  would be negligible. Similarly, the steady-state concentrations of  $\text{SO}_4^{\cdot-}$  were calculated using BA as the probe.

The oxidation contribution of  $^1\text{O}_2$  was calculated according to the previous method with a minor modification.<sup>1</sup> To quantitatively determine the steady-state concentrations of  $^1\text{O}_2$ , furfuryl alcohol (FFA), as a  $^1\text{O}_2$  kinetic probe, was added into the BC/PDS systems with stirring (Figure S10a). FFA residual concentrations were analyzed with HPLC. The steady-state concentration of  $^1\text{O}_2$  was calculated by eqs 1-2.

$$\ln([\text{FFA}]/[\text{FFA}]_0) = -k_{obs}t \quad (1)$$

$$[^1\text{O}_2] = k_{obs}/k_r \quad (2)$$

where  $k_r$  is the first-order rate constant ( $1.2 \times 10^8 \text{ M}^{-1}\text{s}^{-1}$ ) between FFA and  $^1\text{O}_2$ .  $[^1\text{O}_2]$  represents the steady-state concentration of  $^1\text{O}_2$ .

$k_{1\text{O}_2, \text{TCP}}$  is the second-order rate constant of  $^1\text{O}_2$  reacting with TCP, which was calculated by a competitive kinetics experiment (Figure S10 b-d) to estimate the contribution of  $^1\text{O}_2$  (eq 3). 3-methoxy-phenol (MOP) was selected as a competitor because the second-order rate constant (Table S6) with  $^1\text{O}_2$  is comparable to that of TCP. Subsequently, the pseudo-first-order rate constant of the reaction of TCP with  $^1\text{O}_2$  ( $k'_{1\text{O}_2, \text{TCP}}$ ) can be calculated via eq 4. Finally, the contribution ( $R_{1\text{O}_2}$ ) of  $^1\text{O}_2$  was obtained by

190 eq 5.

$$\ln([TCP]/[TCP]_0) = k_{102,TCP}/k_{102,MOP} \times \ln([MOP]/[MOP]_0) \quad (3)$$

$$k'_{102,TCP} = k_{102,TCP}[^1O_2]_{ss} \quad (4)$$

$$R_{102} = k'_{102,TCP}/k_{obs,TCP} \times 100\% \quad (5)$$

191 where  $k_{obs, TCP}$  represents the pseudo-first-order rate constant of TCP in the competitive  
192 experiments.

### 193 **Text S6. Degradation product identification.**

194 To better collect degradation products, the reaction system was expanded 10 times to  
195 50 mM of PDS, 2 g L<sup>-1</sup> of BC800, and 50 mg L<sup>-1</sup> of phenols. After 90 min, the BC800  
196 was collected by centrifugation. The obtained powder was washed with ethanol several  
197 times to get the eluate A, and then the above powder was washed again with toluene to  
198 get the eluate B.

199 LC-MS: The products dissolved in ethanol (i.e. eluate A) were analyzed using an  
200 Agilent 6530 liquid chromatography-mass spectrometry under ESI negative ionization  
201 mode. The mobile phase consisted of methanol/H<sub>2</sub>O (v/v, 80/20) at a flow rate of 0.2  
202 mL min<sup>-1</sup>, and the injection volume of each sample was 20 µL.

203 FTIR: The products dissolved in toluene (i.e. eluate B) were first dried and analyzed  
204 by a NicoLET iS50 FTIR instrument in the wavenumber range of 500-4000 cm<sup>-1</sup>.

205 GPC: The eluate B was first dried, re-dissolved in tetrahydrofuran (THF), and  
206 subsequently analyzed for molecular mass at a WATERS 1525 series gel permeation  
207 chromatography equipped with an RI detector at 40 °C.

208 MALDI-TOF-MS: A Bruker Reflex III matrix-assisted laser desorption/ionization



mass spectrometer was also used for analyzing the properties of the above products dissolved in THF. This MALDI instrument was equipped with a nitrogen laser operated at 337 nm. Samples were prepared by mixing the above products with  $\alpha$ -Cyano-4-hydroxycinnamic acid (used as matrix).

In addition, GPC, LC-MS, and gas chromatography-mass spectrometry (GC-MS) were used to analyze degradation intermediates of aniline, chlorobenzene, and 4-chlorobiphenyl in the BC800/PDS system. The specific experimental procedure is similar to that of phenols.

#### **Text S7. Spectrophotometric determination of PDS.**

At various time intervals, transfer 1 mL of the reaction solution into a glass tube containing 1 mL of KI ( $0.5 \text{ g L}^{-1}$ ) /  $\text{NaHCO}_3$  ( $10 \text{ g L}^{-1}$ ) solution, and dilute to 10 mL with ultrapure water. The obtained mixture was shaken well and reacted for 15 min. The absorbance was measured at 352 nm using an ultraviolet spectrophotometer.

#### **Text S8. Fluorescence labeling of C=O groups.**

Methanol solutions of 115 nM dansyl hydrazine (DH) and 0.1 M HCl were prepared respectively and stored in dark. 30 mL of the DH solution was transferred into a 50 mL flask containing 20 mg BC, and then 1 mL of HCl solution was added as a catalyst. The mixture was placed into an incubator shaker and vibrated at 120 rpm in the dark at 25 °C for 62 hours. After the reaction, the supernatant obtained by centrifugation was collected, and the sediment was rinsed with methanol 5 times. The collected supernatant was diluted up to 200 mL with methanol, and 700  $\mu\text{L}$  of the obtained solution was further diluted to 50 mL with acetone. After 3 hours of the dark reaction, the

fluorescence intensity of the solution was recorded (excitation at 350 nm).

#### **Text S9. Boehm titration.**

0.5 g biochar was mixed with 20 mL base solution (0.05 M Na<sub>2</sub>CO<sub>3</sub> and NaOH) and stirred for 24 h. The mixture was then filtered by a 0.45-μm membrane. 10 mL filtrate (5 mL Na<sub>2</sub>CO<sub>3</sub>) was titrated to pH = 5 as the neutralization point by 0.05 M calibrated HCl solution. The number of phenolic groups ( $n_p$ ) was calculated by the following equations:

$$n_{fb} = c_{HCl}(V_0 - V_t)/m_{BC} \quad (6)$$

$$n_p = n_{f NaOH} - n_{f Na2CO3} \quad (7)$$

where  $n_{fb}$  represents the number of functional groups that the corresponding base reacted with;  $c_{HCl}$  represents the concentration of calibrated HCl solution;  $V_0$  and  $V_t$  represent the volume of HCl solution before and after titration, respectively;  $m_{BC}$  represents the biochar dosage (g).

#### **Text S10. EPR measurements.**

PFRs: The persistent free radicals of BC were detected using a Bruker EPR spectrometer. The freshly prepared BC (5 mg) was added into a quartz capillary tube, and following placed in the detector for recording signal. The specific EPR parameters were as follows: center field of 3513 G, sweep width of 120 G, modulation frequency of 100 kHz, modulation amplitude of 2.0 G, sweep time of 40 s, microwave frequency of 9.85 GHz, and microwave power of 20.37 mW.

ROS: Sulfate radical (SO<sub>4</sub><sup>•-</sup>) and hydroxyl radical (<sup>•</sup>OH) trapping with DMPO were monitored by a Bruker EPR spectrometer in the aqueous solution, while TEMP was

used as the spin trapping agent to detect singlet oxygen ( $^1\text{O}_2$ ). The detection process of superoxide radical ( $\text{O}_2^{\cdot-}$ ) was the same as  $\text{SO}_4^{\cdot-}$  except the solvent changed into pure methanol. Briefly, biochar (10 mg) was introduced into the 5 mL of 1 mM PDS solution to initiate the reaction. At the scheduled time (3 min), 1 mL of the mixture was withdrawn from the suspension of biochar/PDS and was filtered using a 0.45- $\mu\text{m}$  filter. Then, 2 mL of DMPO or TEMP solution (50 mM) was immediately mixed with the filtered sample. After reacting for 1 min, the mixture was loaded in quartz capillary tubes for EPR analysis. The parameters of the EPR instrument were the same as the detection of PFRs.

#### **Text S11. Singlet Oxygen Sensor Green method.**

To assess the role of  $^1\text{O}_2$ , a concentration of 500  $\mu\text{M}$  SOSG was freshly prepared with 300  $\mu\text{L}$  of deoxygenated methanol. The labeling experiment was conducted in a flask with a 10 mL mixture of 0.2  $\text{g L}^{-1}$  BC, 5 mM of PDS, and 5  $\text{mg L}^{-1}$  TCP (if necessary); meanwhile 100  $\mu\text{L}$  of SOSG solution was added into the flask under stirring. After 1 min, a 100  $\mu\text{L}$  sample was withdrawn, diluted to 5 mL using ultrapure water, filtered with a 0.22  $\mu\text{m}$  membrane, and finally analyzed by a fluorescence spectrophotometer. The excitation wavelength was set as 488 nm and the emission wavelength range was 450-650 nm. The depletion of the fluorescence intensity was analyzed by comparing it with or without the addition of pollutants.

#### **Text S12. The examination of $\text{O}_2^{\cdot-}$ by nitro blue tetrazolium.**

Nitro blue tetrazolium ( $\text{NBT}^{2+}$ ) is a common qualitative indicator for the detection of  $\text{O}_2^{\cdot-}$ .<sup>2</sup>  $\text{NBT}^{2+}$  could be reduced by  $\text{O}_2^{\cdot-}$  ( $k=5.88\times 10^4 \text{ M}^{-1} \text{ s}^{-1}$ ) to monoformazan ( $\text{MF}^+$ ,

maximum absorption at 530 nm) and may be further reduced into diformazan (DF, maximum absorption at 560 nm). Herein, 0.01 mM NBT<sup>2+</sup> was used to react with O<sub>2</sub><sup>•-</sup>, and its products were determined by an ultraviolet spectrophotometer. As shown in Figure S3, methanol was used to quench <sup>•</sup>OH and SO<sub>4</sub><sup>•-</sup> but does not affect O<sub>2</sub><sup>•-</sup>. No absorption at either 530 nm or 560 nm was observed in BC/PDS process, indicating the negligible formation of O<sub>2</sub><sup>•-</sup> in this system.

#### **Text S13. Analysis of *in situ* Raman.**

The surface chemical change of biochars during PDS activation was probed using a confocal Raman spectrometer (Labram HR evolution) equipped with a laser emitting at 532 nm. Briefly, 5 mg of biochar was placed on a sheet of glass and pressed into sheets 1 mm thick. PDS solution (20 mM) (and TCP solution, if needed) was then dropped onto the sheet and scanned in the range of 600-1800 cm<sup>-1</sup>. The same method was applied to the PDS solution alone without biochar.

#### **Text S14. Two-chamber galvanic oxidation reactor.**

To validate the proposed electron-transfer process, two individual 100 mL chambers, i.e. anode chamber (20 mg L<sup>-1</sup> TCP) and a cathode chamber (10 mM PDS) were built. The reactor contained biochar wrapped graphite electrode, an Ag/AgCl electrode, a KCl salt bridge, and 50 mM Na<sub>2</sub>SO<sub>4</sub> solution as an electrolyte. The current change during the reaction was monitored by an ammeter, and the two electrodes and the ammeter were connected by copper wires. Samples were collected from the chamber cell at various intervals for chemical analysis.

#### **Text S15. Electrochemical tests.**

The electrochemical measurements were performed with a Bio-logic VMP3 electrochemical workstation in a conventional three-electrode cell at 25 °C. A well-polished glassy carbon electrode (GCE) with a diameter of 4 mm was used as the working electrode. 10 mg of biochar was dispersed into a mixture of 0.25 mL of Nafion<sup>®</sup> solution (5.0 wt %) and 2 mL of isopropanol and then sonicated for 1 h. Then, 10 µL of the mixture was dropped onto a glassy carbon electrode and dried at 60 °C. A platinum wire was used as the counter electrode, while an Ag/AgCl electrode was used as the reference electrode. Solutions were prepared using Milli-Q water.

Chronoamperometry *i-t* curves were obtained at the bias of -0.001 V (vs. Ag/AgCl) using 20 mM PBS solution (pH 7) as the electrolyte. After applying the voltage for 30.0 s, 5 mM PDS was added, then adding 5 mg L<sup>-1</sup> TCP at 60.0 s. Electrochemical impedance spectroscopy was measured at open potential with a scan frequency in the range of 10<sup>5</sup> to 10<sup>-1</sup> Hz.

The dynamic Tafel test was performed with BC800 loaded-GCE as a working electrode and 20 mM PBS as the electrolyte. Meanwhile, PDS and TCP were successively added for comparison. All polarization curves were collected at a scan rate of 2 mV s<sup>-1</sup> to avoid the oxidation-peak effect and to determine the overpotentials at small current densities precisely.

Before an open circuit potential test, the BC loaded-GCE was dipped in 20 mM PBS solution overnight to maintain a stable potential. Then the open circuit potential of BC loaded-GCE was monitored by chronopotentiometry analysis using an Ag/AgCl as the reference electrode. The system can also measure the potential variations at the

electrode with the addition of PDS and TCP.

**Text S16. Biochar molecular modeling and DFT calculations.**

The modeling of biochar is mainly divided into three steps: obtain the preliminary formula according to the characterization results, verify the molecular structure, and determine the final structure. Specifically, from the results of the ultimate analysis (Table S8), the dry weight of BC500 and BC800 contain 57.2 and 65.1% carbon, 2.6 and 1.3% hydrogen, and about 16.9 and 8.9% oxygen, respectively, with trace amounts of nitrogen and sulfur. To simplify the biochar model, nitrogen and sulfur were not considered in the molecular construction, and thereby the initial formula of the conceptual model was normalized to one carbon atom:  $C_1H_xO_y$ . The normalization coefficients were then calculated from the aforesaid elemental compositions and elemental molecular weights. The derived empirical formulas of BC500 and BC800 are  $C_1H_{0.55}O_{0.22}$  and  $C_1H_{0.24}O_{0.10}$ , respectively. Taking advantage of the quantitative relationship between the H/C atomic ratio and the aromatic cluster size established by Xiao et al.,<sup>3</sup> the corresponding aromatic clusters of BC500 and BC800 were distributed in approximately 3\*3 and 6\*6 rectangles, respectively.

FTIR spectrum (Figure S15) of biochars shows that the oxygen-containing groups exist mainly in the form of phenolic hydroxyl groups and ether groups. Since the saturated fatty ethers are not stable, the cyclic ethers (i.e. phenoxy, phenhydroxy, and methoxy groups) are the dominant groups. The weak peaks located around 2900 and 1460  $cm^{-1}$  indicated the presence of a small amount of aliphatic  $CH_x$ . Moreover, 880 and 800  $cm^{-1}$  suggested one adjacent H deformation and two adjacent H deformations,

respectively.

Solid-state  $^{13}\text{C}$  NMR spectra of BC500/800 showed a strong signal at about 128 ppm, which can be attributed to aromatic carbon, and the peak around 152 ppm was assigned to oxy-aromatic carbon.<sup>4</sup> Moreover, the signals in 15-22 and 29-35 ppm regions indicate the presence of methyl and/or methylene groups.<sup>5</sup>

From the results of FTIR and NMR analysis, the main functional groups within the macromolecular structure of biochars can be derived. Combining the biochar formulas described above (i.e.,  $\text{C}_1\text{H}_{0.55}\text{O}_{0.22}$  and  $\text{C}_1\text{H}_{0.24}\text{O}_{0.10}$ ), a 3D molecular model of biochar was built using ChemDraw software. The carbon chemical shift of the obtained molecular model was calculated, and the simulated spectrum was checked by MestReNova software. By comparing the actual and calculated  $^{13}\text{C}$  NMR spectra, the model was repeatedly optimized until the calculated spectrum was consistent with the experimental one, thus ensuring the authenticity and rationality of the model. The final empirical formulas of BC500 and BC800 are  $\text{C}_{28}\text{H}_{18}\text{O}_5$  and  $\text{C}_{70}\text{H}_{26}\text{O}_6$ , respectively. This structure model is used for further DFT calculations.

The first-principles calculations were carried out using the Vienna ab initio simulation package (VASP) with the projector augmented wave (PAW) method. Spin-polarization density functional theory (DFT) calculations were performed using the Perdew-Burke-Ernzerhof (PBE) functional.<sup>6-8</sup> We chose PAW potentials to describe the ionic cores and took valence electrons into account using a plane-wave basis set with a kinetic energy cutoff of 400 eV.<sup>9,10</sup> Partial occupancies of the Kohn–Sham orbitals were allowed using the Gaussian smearing method with a width of 0.05 eV. Geometry

363 optimization was considered convergent when the maximum atomic force was smaller  
364 than 0.05 eV Å<sup>-1</sup>. The vacuum spacing in a direction perpendicular to the plane of the  
365 structure was 15 Å. The Brillouin zone was sampled using a (3×3×1) Monkhorst-Pack  
366 k-point grid. The configurations of O<sub>8</sub>S<sub>2</sub> and TCP were optimized at the ωB97XD/def2-  
367 SVP level.<sup>11</sup> All geometry optimizations including the implicit solvent effect with SMD  
368 were implemented by the Gaussian package and the harmonic frequency calculations  
369 were carried out at the same level of theory to confirm that all structures have no  
370 imaginary frequency.<sup>12,13</sup> The highest occupied molecular orbital (HOMO) and lowest  
371 unoccupied molecular orbital (LUMO) maps of all configurations were rendered by  
372 using Visual Molecular Dynamics (VMD) software based on the files exported from  
373 Multiwfn 3.7 (dev) code with 0.02 isovalue.<sup>14,15</sup>



## Part S2. Supplementary Tables

**Table S1.** Summary of the chronopotentiometry data according to the literature.

Catalyst	[Oxidant] (mM)	[Pollutant] (mM)	Potential of complex (V)	$E_{1/2}$ of pollutant <sup>a</sup> (V)	$k_{\text{obs}}$ (min <sup>-1</sup> )	Ref.
CNTs	[PDS] = 1	[Methoxy-phenol] = 0.1	0.65	0.32	0.122	16
		[Nitrophenol] = 0.1		0.78	0.004	
Mn <sub>2</sub> O <sub>3</sub> -Fe <sub>2</sub> O <sub>3</sub>	[PMS] = 0.5	[Nitrophenol] = 0.1	0.91	0.78	0.005	17
sludge biochar	[PMS] = 5	[Nitrophenol] = 0.1	1.02	0.78	0.005	18
N-doped carbon	[PMS] = 6.5	[Sulfamethoxazole] = 0.08	1.09	1.38	0.35	19

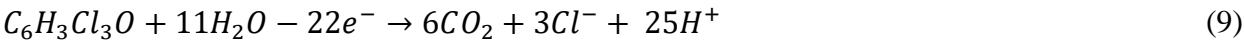
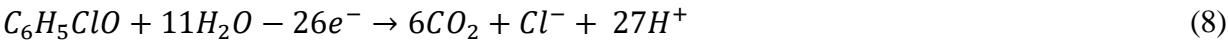
<sup>a</sup> Half-wave potentials ( $E_{1/2}$ ) values reflect the potential for the first electron oxidation step, which has been widely used as a measurement for organic compounds' susceptibility to oxidation.

Currently, the generally accepted electron-transfer mechanism is the metastable surface complex oxidation proposed by Zhang's group. Persulfate and pollutants are first co-adsorbed onto the catalyst surface. Then, the adsorbed persulfate is activated to form a catalyst-persulfate complex, thereby elevating the overall redox potential of the catalyst. Finally, when the potential of the complex exceeds the oxidation potential of the pollutant, the complex will abstract electrons from the vulnerable pollutants to fulfill the oxidation. For example, methoxy-phenol can be easily oxidized (0.65 V > 0.32 V) in the CNTs/PDS system, while nitrophenol is difficult to be oxidized (0.65 V < 0.78 V).<sup>16</sup> However, we noticed two cases that could not be explained by the above theory. 1) In several other studies by Zhang et al.,<sup>17,18</sup> even though the complex potential far exceeds the oxidation potential (i.e. 0.91 V or 1.02 V > 0.78 V), the pollutants are still difficult to remove in the Mn<sub>2</sub>O<sub>3</sub>-Fe<sub>2</sub>O<sub>3</sub>/PMS and sludge biochar/PMS systems. 2) We also observed in the N-doped carbon/PMS system reported by Wang et al. that the pollutants can be effectively removed (the roles of radicals and <sup>1</sup>O<sub>2</sub> were excluded) even if the potential of the complex is lower than that of the pollutants (i.e. 1.09 V < 1.38 V).<sup>19</sup> These conflicting results suggest that the potential of the complex is not the only factor determining the degradation rate in electron transfer-dominated oxidation systems.

**Table S2.** The electron-equivalent data calculated according to the literature and this study.

Catalyst	[Pollutant] (mM)	TOC removal (%)	Given $e^-$ (mM) <sup>a</sup>	[oxidant] (mM)	Obtained $e^-$ (mM) <sup>b</sup>	$e^-$ utilization (%) <sup>c</sup>	Ref.
N-doped carbon	[4-CP] = 0.156	53	1.557	[PMS] = 0.033	0.065	-	20
Activated carbon	[Phenol] = 0.531	86	12.780	[PDS] = 2.66	5.313	-	21
Biochar	[Aniline] = 0.107	52	1.639	[PDS] = 0.378	0.756	-	22
Fe <sub>3</sub> C@NCNTs/GNS	[Bisphenol A] = 0.088	65	3.489	[PMS] = 0.325	0.650	-	23
CNTs	[2,4-DCP] = 0.031	40	0.167	[PDS] = 0.031	0.062	-	24
BC800	[2,4,6-TCP] = 0.025	77	0.363	[PDS] = 0.1	0.2	182	This study
Heat (70 °C)	[Bisphenol A] = 0.088	69	4.245	[PDS] = 10	20	21	25
UV	[Phenol] = 0.5	63	8.820	[PDS] = 84	168	5	26

<sup>a</sup> The given electron equivalent of pollutant is calculated according to the mineralization rate (excluding adsorption quantity). Take N-doped porous carbon/4-CP as an example, the given  $e^-$  = ([4-CP]<sub>initial</sub> - [4-CP]<sub>adsorbed</sub>) × TOC removal × 26 = (0.156-0.043) × 53% × 26 = 1.557 (eq 8). And for the BC800/TCP, the given  $e^-$  = ([TCP]<sub>initial</sub> - [TCP]<sub>adsorbed</sub>) × TOC removal × 22 = (0.025-0.0036) × 77% × 22 = 0.363 (eq 9).



<sup>b</sup> The obtained electron equivalent of oxidant is calculated according to its actual dosage. 1 mol PDS/PMS accepts 2 mol  $e^-$  during oxidation.

<sup>c</sup> Electron utilization efficiency is calculated by the ratio of the given electron equivalent of pollutant/obtained electron equivalent of oxidant.

In this study, the electron utilization efficiency of the BC800/PDS system is calculated as (0.363/0.2) × 100% = 182%, which is much higher than the electron utilization efficiency in homogeneous persulfate oxidation (e.g. heat and UV activation).<sup>22,23</sup> This result highlights the potential benefits of heterogeneous biochar-catalyzed PDS oxidation for organic pollutant removal.

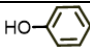
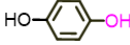
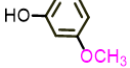
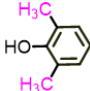

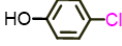
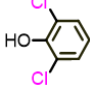
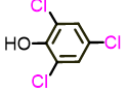
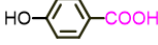

401 **Table S3.** Detection parameters of HPLC.

Compound	Mobile phase		Wavelength (nm)	Retention time (min)
	A (%)	B (%)		
Phenol (PE)	70	30	270	4.1
Hydroquinone (HQ)	20	80	285	7.6
4-chlorophenol (CP)	70	30	280	8.8
4-nitrophenol (NP)	70	30	254	7.4
4-methylphenol (MP)	70	30	310	12.1
2,6-dimethylphenol (DMP)	60	40	270	9.7
3-methoxy-phenol (MOP)	70	30	226	4.0
2,6-dichlorophenol (DCP)	90	10	280	7.5
4-hydroxybenzoic acid (HBA)	50	50	250	9.1
2,4,6-trichlorophenol (TCP)	70	30	284	11.6
Furfuryl alcohol (FFA)	70	30	219	3.5
Nitrobenzene (NB)	70	30	254	7.5
Benzoic acid (BA)	55	45	235	4.6

402 Mobile phase A: methanol; mobile phase B: water (1% acetic acid); column  
 403 temperature: 30 °C; flow rate: 1.0 mL min<sup>-1</sup>.

404

405 **Table S4.** Observed degradation rate constants  $k_{\text{obs}}$  of phenolic compounds.

Compound	Structure	Substituent <sup>a</sup>	$k_{\text{obs,BC400}}$	$k_{\text{obs,BC500}}$	$k_{\text{obs,BC800}}$
PE		-	0.0011	0.0014	0.0035
HQ		strong EDG	0.0026	0.0019	0.1189
MOP		strong EDG	0.0012	0.0009	0.0261
DMP		strong EDG	0.0018	0.0032	0.0731
MP		weak EDG	0.0021	0.0027	0.0713
CP		weak EWG	0.0014	0.0020	0.0085
DCP		weak EWG	0.0009	0.0022	0.0146
TCP		weak EWG	0.0024	0.0034	0.1169
HBA		median EWG	0.0009	0.0015	0.0027
NP		strong EWG	0.0011	0.0017	0.0018

406 <sup>a</sup>EDG: electron-donating group; EWG: electron-withdrawing group.

407

408 This substrate-dependent reactivity of the BC800/PDS system cannot be explained  
 409 by the discrepancy in reaction rates between radicals and contaminants. For example,  
 410 though MP and PE deliver similar second-order kinetic constants ( $k_{\text{SO}_4^{\bullet-}, \text{MP}} = 6.1 \times 10^9$   
 411  $\text{M}^{-1} \text{s}^{-1}$ ,  $k_{\text{SO}_4^{\bullet-}, \text{PE}} = 6.2 \times 10^9 \text{M}^{-1} \text{s}^{-1}$ ,  $k_{\text{OH}, \text{MP}} = 2.2 \times 10^{10} \text{M}^{-1} \text{s}^{-1}$ , and  $k_{\text{OH}, \text{PE}} = 1.9 \times 10^{10}$   
 412  $\text{M}^{-1} \text{s}^{-1}$ ),<sup>27, 28</sup> the latter was refractory to degrade in this system. We thus attribute this  
 413 unique selectivity to electron-transfer nonradicals, whose oxidation pathways are  
 414 widely reported to be susceptible to the electronic effects of substituents.<sup>29</sup>

415 **Table S5.** Open circuit potential (OCP) data of the three biochars.

Samples	OCP <sup>a</sup>									
	V <sub>+PDS</sub>	Δ <sub>E+PDS</sub>	Δ <sub>E+TCP</sub>	Δ <sub>E+HQ</sub> <sup>b</sup>	Δ <sub>E+MOP</sub> <sup>b</sup>	Δ <sub>E+DMP</sub> <sup>b</sup>	Δ <sub>E+PE</sub> <sup>b</sup>	Δ <sub>E+CP</sub> <sup>b</sup>	Δ <sub>E+DCP</sub> <sup>b</sup>	Δ <sub>E+NP</sub> <sup>b</sup>
BC400	0.43	0.192	-0.003	-	-	-	-	-	-	-
BC500	0.46	0.214	-0.005	-	-	-	-	-	-	-
BC800	0.67	0.407	-0.056	-0.135	-0.031	-0.045	-0.018	-0.031	-0.015	-0.010

416 <sup>a</sup> Reaction conditions: [PDS]<sub>0</sub> = 5 mM, [Phenols]<sub>0</sub> = 5 mg L<sup>-1</sup>, 25 °C.

417 <sup>b</sup> The change of potential when the contaminant is added alone.

418

419

420 **Table S6.** Second-order rate constants (M<sup>-1</sup> s<sup>-1</sup>) between ROS and probe compounds.

Compound	•OH	SO <sub>4</sub> <sup>•-</sup>	<sup>1</sup> O <sub>2</sub>
Nitrobenzene	4.7 × 10 <sup>9, 30</sup>	< 10 <sup>6, 31</sup>	-
Benzoic acid	2.1 × 10 <sup>9, 32</sup>	1.2 × 10 <sup>9, 31</sup>	-
3-methoxy-phenol (MOP)	-	-	1.3 × 10 <sup>7, 33</sup>
TCP	5.4 × 10 <sup>9, 34</sup>	2.9 × 10 <sup>9, 35</sup>	1.7 × 10 <sup>7, 33</sup>

421

**Table S7.** Quantitative analysis of O species in the biochars based on O 1s XPS spectra.

Samples	Attribution	Binding energy (eV)	FWHM (eV)	Relative content (%)
BC400	–OH	531.1	1.7	9.54
	C–O	532.2	1.6	8.03
	C=O	533.2	1.6	5.37
BC500	–OH	531.1	1.5	5.45
	C–O	532.2	1.7	8.29
	C=O	533.2	1.6	5.58
BC800	–OH	531.1	1.5	5.55
	C–O	532.2	1.5	6.22
	C=O	533.2	1.5	2.82
oBC400	–OH	531.1	1.6	7.27
	C–O	532.2	1.7	19.40
	C=O	533.2	1.7	7.44
rBC400	–OH	531.1	1.5	7.83
	C–O	532.2	1.6	8.36
	C=O	533.2	1.6	4.39
Used BC400	–OH	531.1	1.5	5.00
	C–O	532.2	1.5	12.43
	C=O	533.2	1.6	7.31
Used BC500	–OH	531.1	1.5	4.11
	C–O	532.2	1.6	11.54
	C=O	533.2	1.5	7.14
Used BC800	–OH	531.1	1.7	2.99

	C–O	532.2	1.6	8.02
	C=O	533.2	1.7	3.92
	–OH	531.1	1.7	5.00
Used oBC400	C–O	532.2	1.5	15.85
	C=O	533.2	1.5	8.80
	–OH	531.1	1.5	2.58
Used rBC400	C–O	532.2	1.5	13.96
	C=O	533.2	1.6	6.17

**Table S8.** Elemental compositions of different biochars as well as their PFR properties (i.e., g-factor), C=O, and phenolic –OH contents.

	BC400	BC500	BC800	oBC400	rBC400
C 1s (at. %) <sup>a</sup>	77.06	80.68	85.41	65.89	79.42
O 1s (at. %) <sup>a</sup>	22.94	19.32	14.59	34.11	20.58
C 1s (at. %) <sup>b</sup>	78.91	79.22	85.06	70.34	77.30
O 1s (at. %) <sup>b</sup>	21.09	20.78	14.94	29.66	22.70
Ash (wt. %)	18.6	22.5	23.8	16.2	19.5
C (wt. %)	54.6	57.2	65.1	49.4	57.9
H (wt. %)	2.8	2.6	1.3	3.3	3.6
O (wt. %)	23.1	16.9	8.9	30.2	17.8
N (wt. %)	0.7	0.7	0.6	0.7	0.9
S (wt. %)	0.2	0.1	0.3	0.2	0.3
H/C (%)	0.62	0.55	0.24	0.80	0.75
O/C (%)	0.32	0.22	0.10	0.46	0.23
g-factor <sup>c</sup>	2.0043	2.0041	ND	2.0045	2.0042
C=O (groups g <sup>-1</sup> ) <sup>d</sup>	4.3×10 <sup>7</sup>	8.6×10 <sup>7</sup>	3.5×10 <sup>7</sup>	13.1×10 <sup>7</sup>	2.0×10 <sup>7</sup>
phenolic –OH (mmol g <sup>-1</sup> )	0.16	0.08	0.01	0.12	0.30

<sup>a</sup> Obtained by XPS analysis of fresh biochars;

<sup>b</sup> Obtained by XPS analysis of used biochars after ethanol/benzene/water washing.

<sup>c</sup> g-factor < 2.0030: carbon-centered PFRs;

g-factor of 2.0030–2.0040: carbon-centered PFRs with an adjacent oxygen atom;

g-factors > 2.0040: oxygen-centered PFRs.<sup>36</sup>

<sup>d</sup> Determined by the dansyl hydrazine fluorescence labeling method.

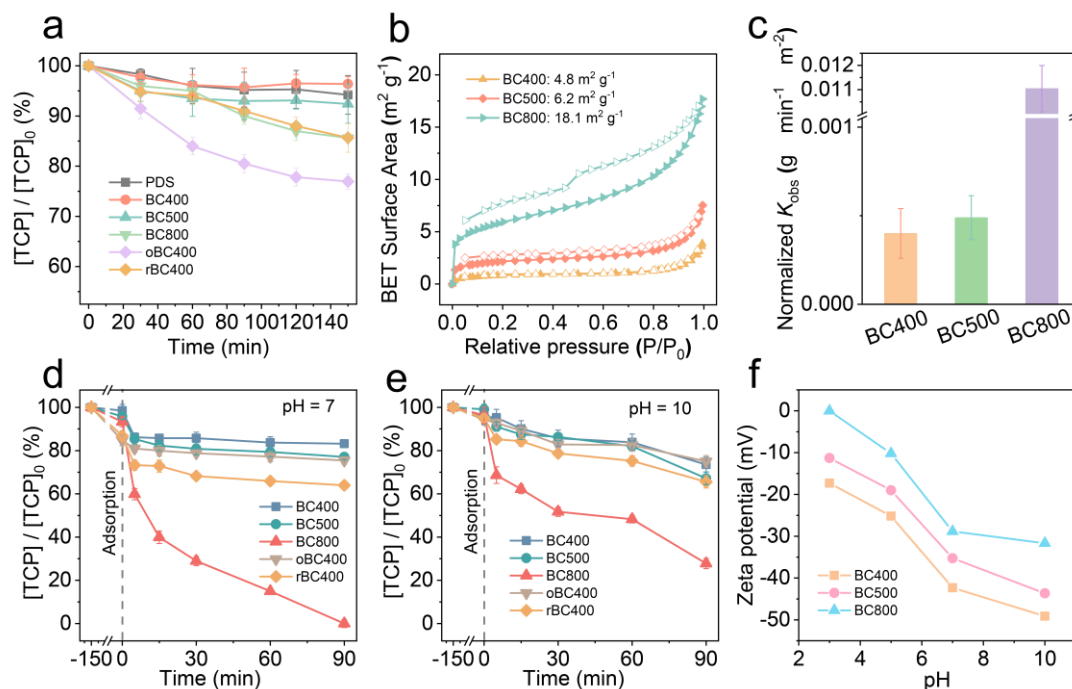


432 **Table S9.** Verification of the simulated biochar models.

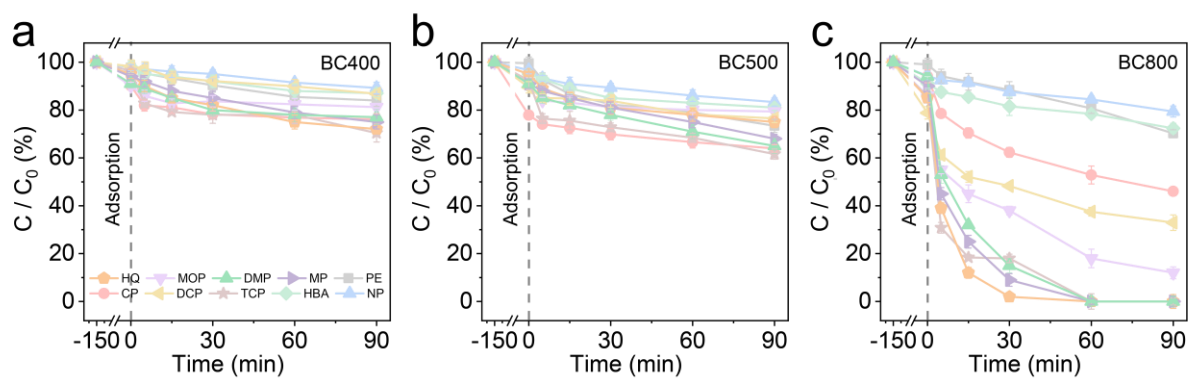
Samples	Elemental composition (%)			Empirical Formula
	C	H	O	
BC500	74.7	3.4	21.9	$C_1H_{0.55}O_{0.22}$
Simulated BC500	77.4	4.1	18.5	$C_{28}H_{18}O_5$
BC800	86.7	1.7	11.6	$C_1H_{0.24}O_{0.10}$
Simulated BC800	88.5	2.7	8.8	$C_{70}H_{26}O_6$

433

## Part S3. Supplementary Figures



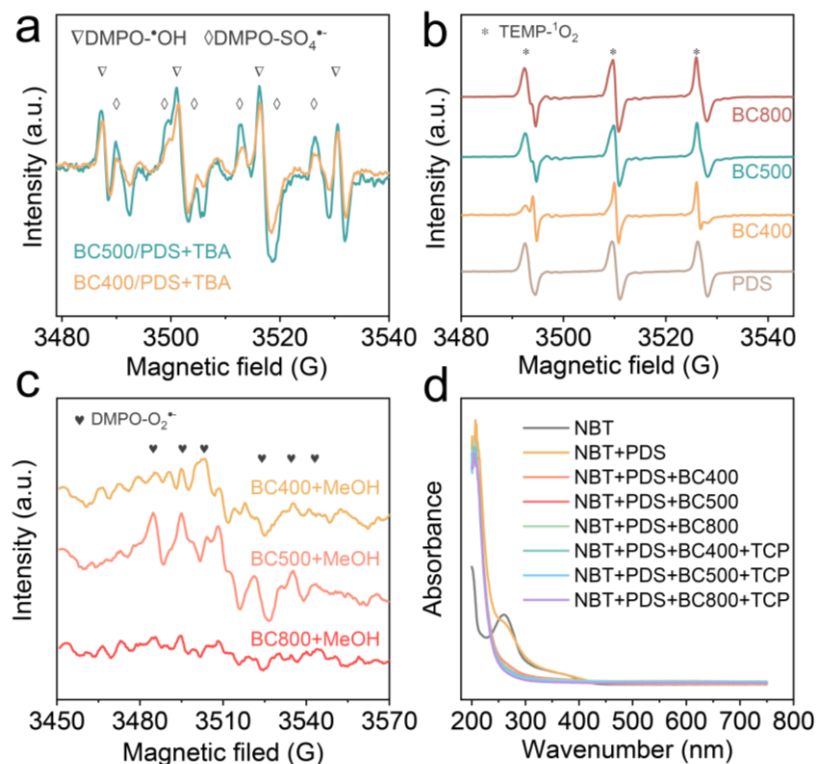
**Figure S1.** (a) TCP removal by PDS oxidation and biochars adsorption, respectively. (b) Nitrogen adsorption-desorption isotherms (filled and open symbols correspond to the adsorption and desorption branches, respectively). (c) Normalized degradation rate constants by the specific surface area. Time profiles of TCP removal at pH = 7 and 10 (d and e) in the biochar/PDS systems. (f) The zeta potential-pH curves for the biochars produced at different pyrolysis temperatures. (Reaction conditions:  $[PDS]_0 = 5 \text{ mM}$ ,  $[biochar] = 0.2 \text{ g L}^{-1}$ ,  $25 \text{ }^\circ\text{C}$ .)



**Figure S2.** Degradation profiles of various phenols in the biochar/PDS system.

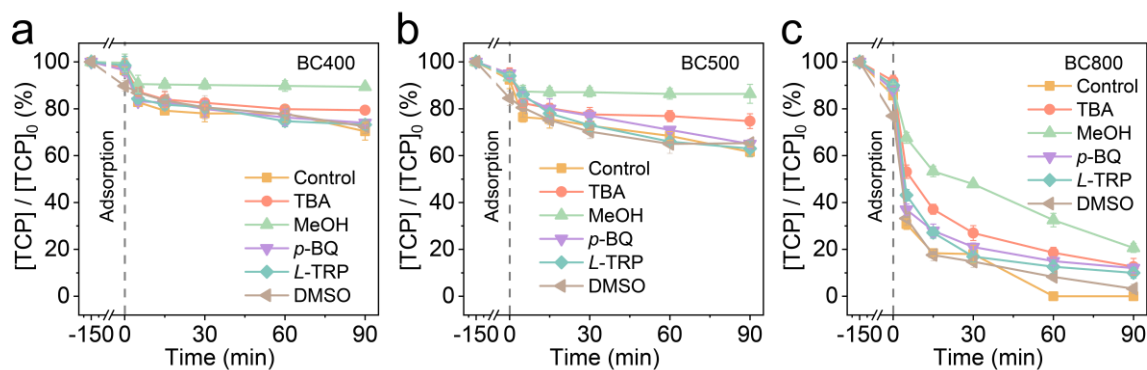
(Reaction conditions:  $[PDS]_0 = 5 \text{ mM}$ ,  $[\text{biochar}] = 0.2 \text{ g L}^{-1}$ ,  $[\text{phenols}]_0 = 5 \text{ mg L}^{-1}$ ,

$25^\circ\text{C}$ .)

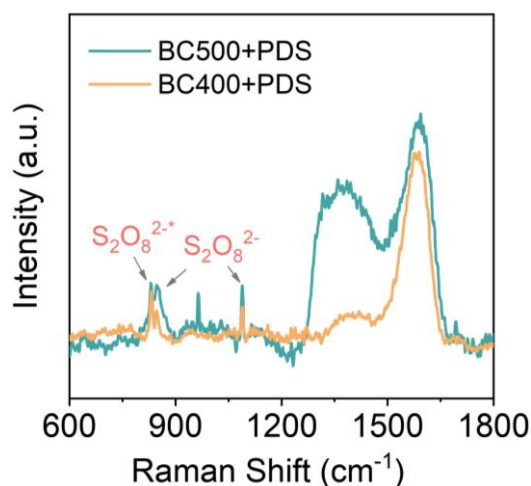


**Figure S3.** (a) EPR spectra for the BC400 and BC500 activated PDS systems in water/tert-butyl alcohol (v/v = 1). (b) EPR signals of TEMP adducts. (c) DMPO-trapped EPR spectroscopy analysis using MeOH as a solvent, and (d) UV-vis spectra for the examination of NBT $^{2+}$ . (Reaction conditions: [PDS] $_0$  = 5 mM, [biochar] = 0.2 g L $^{-1}$ , [TCP] $_0$  = 5 mg L $^{-1}$ , [DMPO] = 25 mM, [NBT] = 0.01 mM, 25 °C.

To show the DMPO-SO $_4^{\cdot-}$  signal more clearly, TBA as a scavenger for  $\cdot$ OH was added into the activation system prior to EPR tests. As depicted in Figure S3a, remarkable signals of DMPO-SO $_4^{\cdot-}$  were detected.

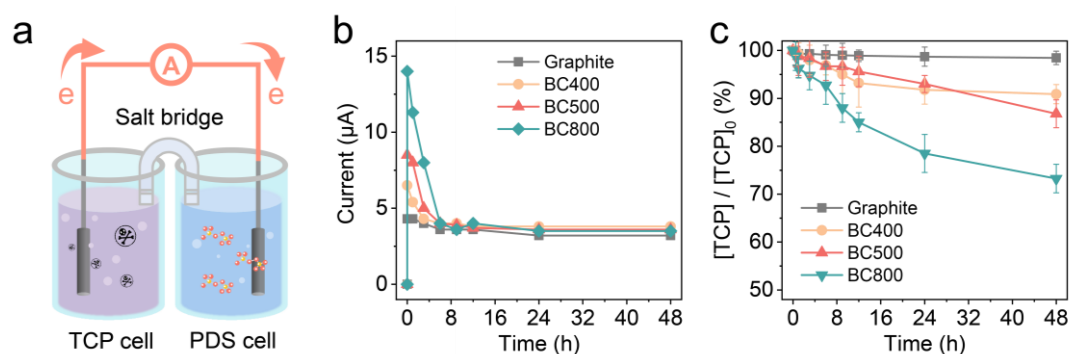


**Figure S4.** Quenching effects of different scavengers. (Reaction conditions:  $[PDS]_0 = 5$  mM,  $[biochar] = 0.2$  g L<sup>-1</sup>,  $[TCP]_0 = 5$  mg L<sup>-1</sup>,  $[Tert-butyl\ alcohol, TBA] = [Methanol, MeOH] = 0.5$  M,  $[p-benzoquinone, p-BQ] = 10$  mM,  $[L-tryptophan, L-TRP] = 10$  mM,  $[Dimethyl\ sulfoxide, DMSO] = 10$  mM, 25 °C.)

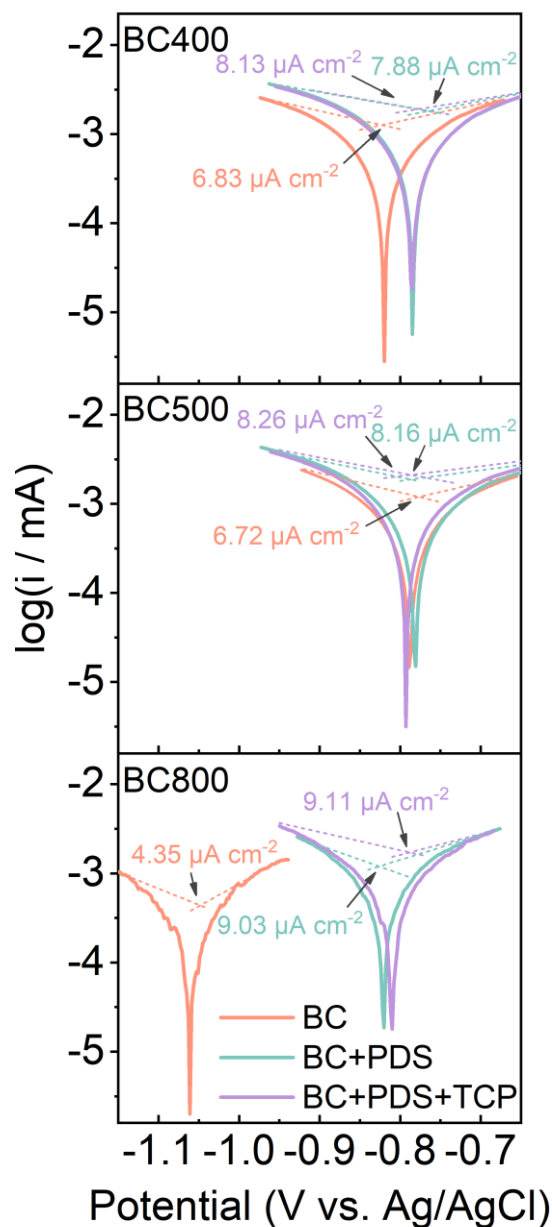


**Figure S5.** *In situ* Raman spectra of BC400 and BC500 combined with PDS ( $[PDS]_0 = 20 \text{ mM}$ ,  $[biochar] = 5 \text{ g L}^{-1}$ , solution pH without adjustment).

The Raman results indicated that active complexes were also formed in the BC400 and BC500/PDS systems, which was consistent with the OCP results that the addition of PDS elevated the potential of biochar-coated electrodes, among which the BC800 system has the highest potential.

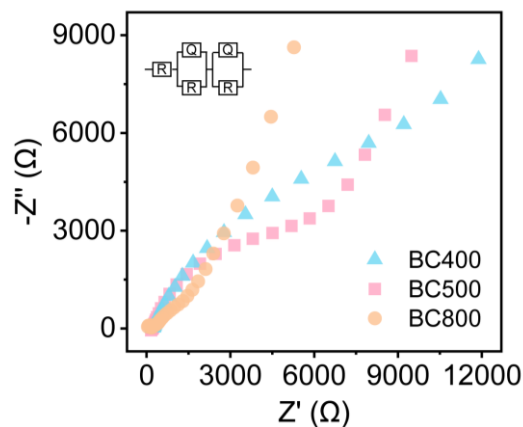


**Figure S6.** (a) Two-chamber galvanic oxidation reactor. (b) Current formation and (c) TCP degradation in the reactor ( $[PDS]_0 = 10 \text{ mM}$ ,  $[TCP]_0 = 20 \text{ mg L}^{-1}$ ,  $25 \text{ }^{\circ}\text{C}$ ).

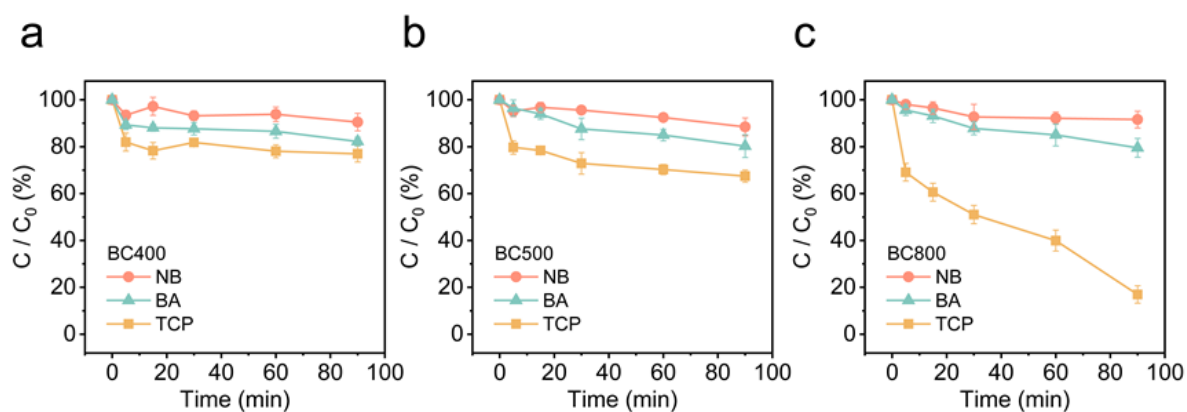


**Figure S7.** Dynamic Tafel curves obtained using biochars-coated GCE as the working electrode.

The exchange current density of BC800/PDS ( $9.03 \mu\text{A cm}^{-2}$ ) was higher than that of BC400/ and BC500/PDS, indicating that the PDS activation by BC800 had a lower activation barrier and higher electron-transfer rate than that by BC400 and BC500.

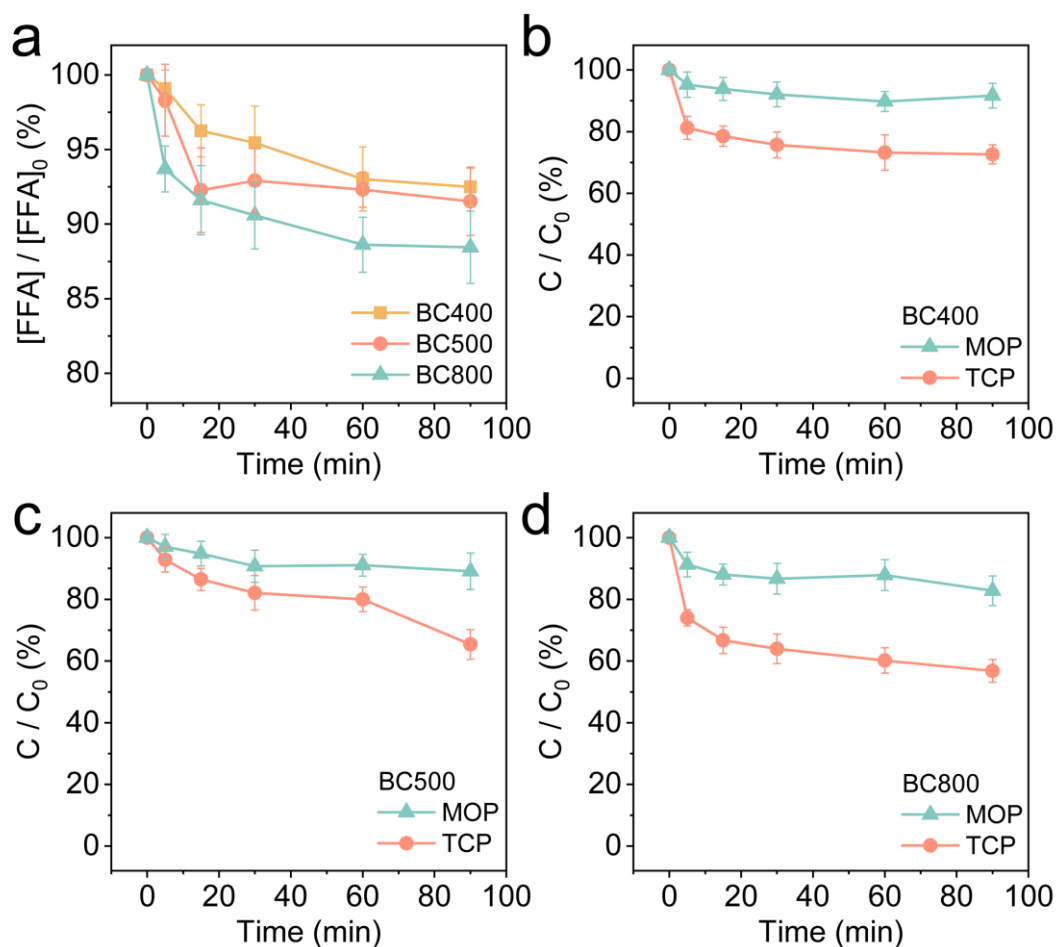


**Figure S8.** Electrochemical impedance spectroscopy Nyquist plots.

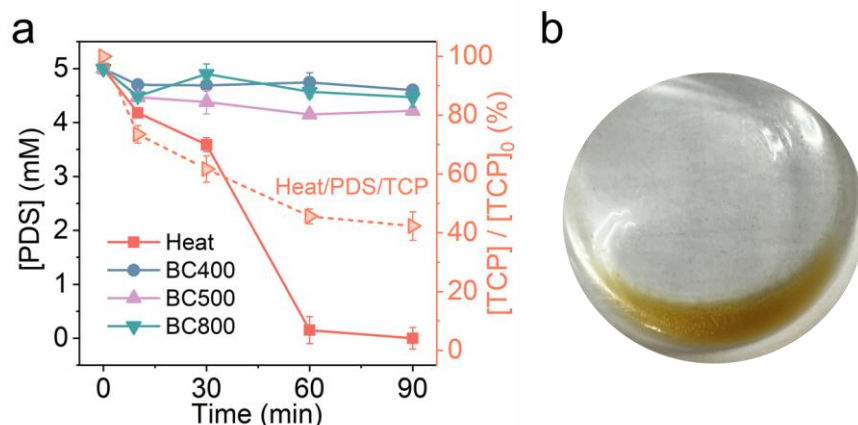


**Figure S9.** Degradation of TCP, nitrobenzene (NB), and benzoic acid (BA) in different systems. (Reaction conditions:  $[PDS]_0 = 5 \text{ mM}$ ,  $[\text{biochar}] = 0.2 \text{ g L}^{-1}$ ,  $[\text{TCP}]_0 = 5 \text{ mg L}^{-1}$ ,  $[\text{BA}]_0 = [\text{NB}]_0 = 0.01 \text{ mM}$ ,  $25^\circ\text{C}$ .)



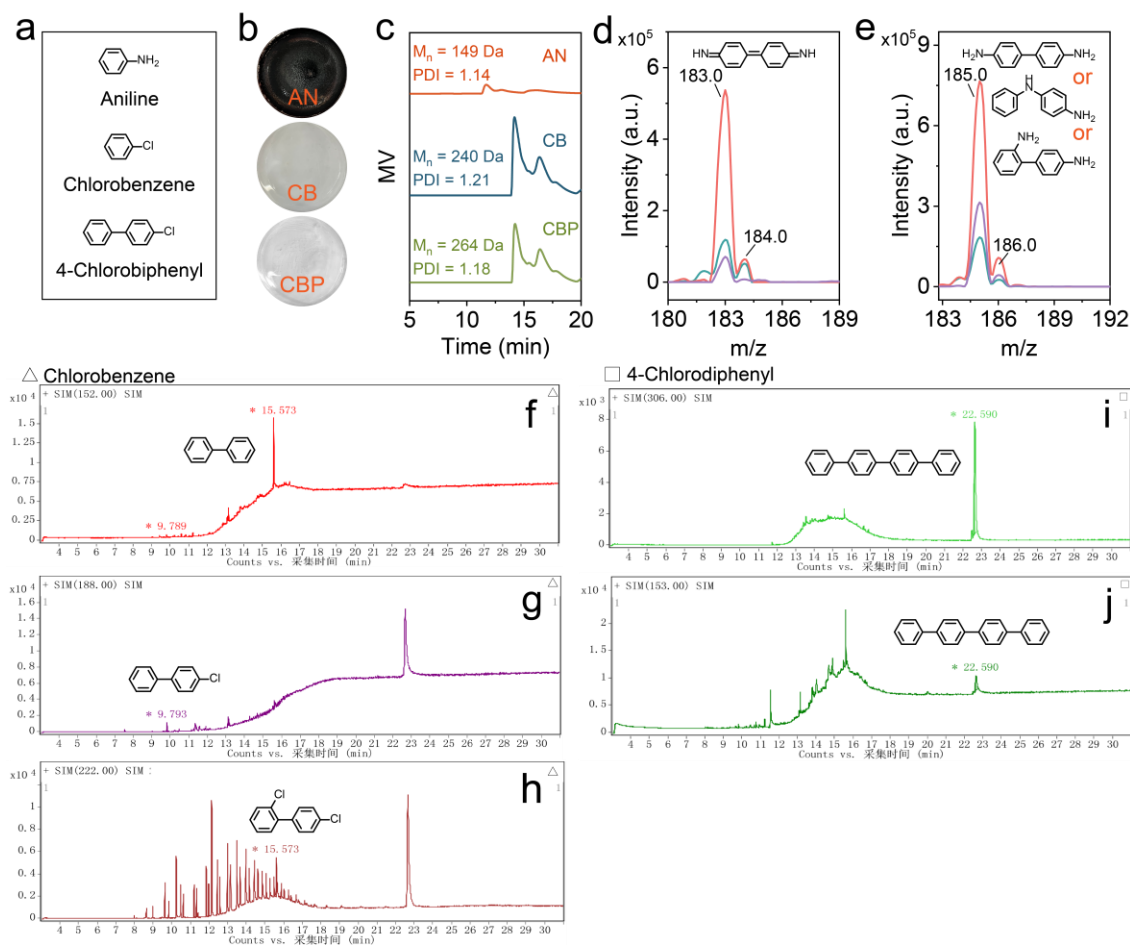


**Figure S10.** (a) Time course of furfuryl alcohol (FFA) removal. (b-d) Competitive degradation between TCP and 3-methoxy-phenol (MOP). (Reaction conditions:  $[PDS]_0 = 5$  mM,  $[biochar] = 0.2$  g L<sup>-1</sup>,  $[TCP]_0 = [MOP]_0 = 0.025$  mM,  $[FFA]_0 = 2$  mM, 25 °C.)



**Figure S11.** (a) Concentration changes of PDS in biochar and thermal activation systems, and TCP degradation (dashed line) in thermal activation system. (Reaction conditions:  $[PDS]_0 = 5 \text{ mM}$ ,  $[\text{biochar}] = 0.2 \text{ g L}^{-1}$ ,  $[TCP]_0 = 5 \text{ mg L}^{-1}$ , heating temperature =  $70 \text{ }^{\circ}\text{C}$ .) (b) Photograph of the gelatinous substances in toluene after drying.

The BC800 system showed a moderate PDS consumption than the other biochars (Figure S11a), that is,  $\text{BC500} > \text{BC800} > \text{BC400}$ , consistent with the order of  $\text{SO}_4^{\cdot-}$  yield. Notably, compared with all biochars, the thermal activation showed a more rapid PDS decline over reaction time and completely consumed the oxidant within 90 min, but exhibited a lower oxidation efficiency than BC800 (Figure S11a). These results emphasize the advantages of higher electron utilization efficiency in BC800/PDS systems dominated by nonradical oxidation.



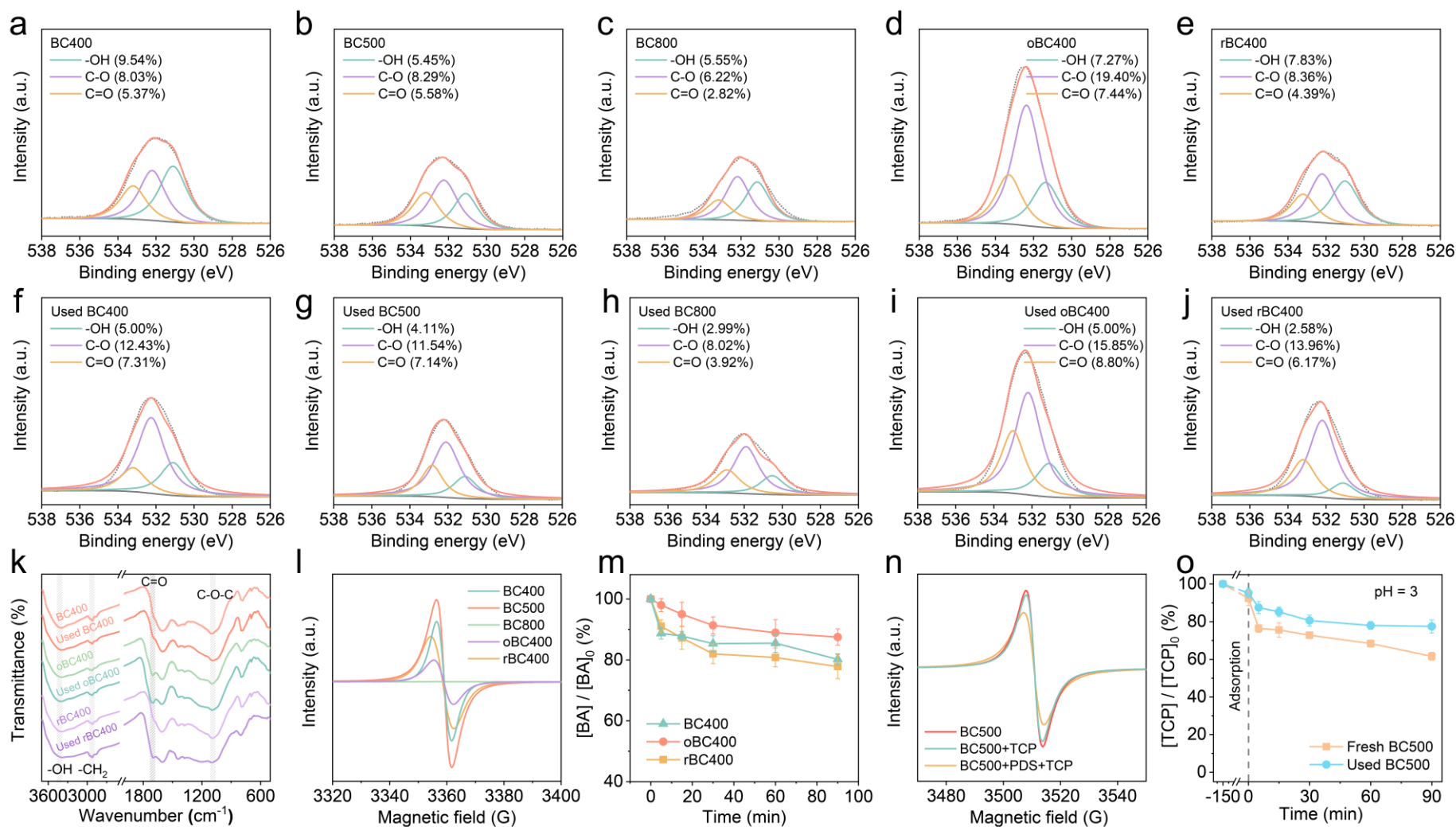
**Figure S12.** (a) Structural formulas for the selected pollutants. (b) Photographs of degradation products dissolved in toluene. (c) Gel permeation chromatogram of the products eluted by toluene. (d, e) LC-MS spectrum of the products of aniline after ethanol elution. GC-MS chromatograms of the products in the (f-h) chlorobenzene/BC800/PDS and (i, j) 4-chlorobiphenyl/BC800/PDS systems. (Reaction conditions:  $[PDS]_0 = 50 \text{ mM}$ ,  $[biochar] = 2 \text{ g L}^{-1}$ ,  $[AN]_0 = [CB] = [CBP] = 15 \text{ mM}$ .)

GPC results suggested that similar to phenols, phenyl oligomers were also found in the aniline (AN), chlorobenzene (CB), and 4-chlorobiphenyl (CBP) reaction systems. It is worth noting that the yield of degradation products (Figure S12b) of aniline dissolved in toluene is significantly higher than that of the latter two at the same dosage.

Combined with the aforementioned selective oxidation results (Table S4), we speculated that the benzene ring containing EDG (e.g., -NH<sub>2</sub>) is more prone to nonradical oxidation than the benzene ring bearing EWG (e.g., -Cl), thus facilitating the formation of oligomers via polymerization reactions. Furthermore, mass spectrometry results suggested that various dimeric products were also generated on the ethanol-washed biochar surface. These results substantially broaden the applicability of the proposed ‘selective oxidation\_adhesion’ mechanism in non-phenolic pollutants.



**Figure S13.** The reversible transformation of RAMs on biochars.



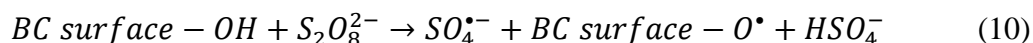
539

540 **Figure S14.** Fitted curves of high-resolution XPS O1s spectrum of (a-e) fresh biochars and (f-j) used biochars after washing. (k) FTIR spectra and  
 541 (l) PFRs intensity of biochars with tuned RAM compositions. (m) Degradation of benzoic acid (BA) in different systems. (Reaction conditions:  
 542 [PDS]<sub>0</sub> = 5 mM, [biochar] = 0.2 g L<sup>-1</sup>, [BA]<sub>0</sub> = 0.01 mM, 25 °C.) (n) Changes in the PFRs signals and (o) TCP removal efficiencies of BC500  
 543 before and after the reaction. (Reaction conditions: [PDS]<sub>0</sub> = 5 mM, [biochar] = 0.2 g L<sup>-1</sup>, [TCP]<sub>0</sub> = 5 mg L<sup>-1</sup>, 25 °C.)

Herein, H<sub>2</sub>O<sub>2</sub> oxidation was adopted to tune phenolic –OH, and semiquinone-type PFRs into quinoid C=O. From the O 1s XPS spectra (Table S7 and Figures S14a,d), the quinoid C=O content increased from 5.37 to 7.44%. Moreover, Table S8 shows that the surface concentration of C=O groups rapidly soared from  $4.3 \times 10^7$  to  $13.1 \times 10^7$  groups g<sup>-1</sup> based on fluorescence labeling measurement. The FTIR spectra also recorded an enhanced intensity of quinoid C=O signal for oBC400 at ~1700 cm<sup>-1</sup> (Figure S14k). Accompanied by the increased quinoid C=O, both phenolic –OH (from 0.16 to 0.12 mmol g<sup>-1</sup>, Table S8) and oxygen-centered PFRs dropped considerably (Figure S14l). These observations confirm the conversion of reduced RAMs (i.e., phenolic -OH and semiquinone-type PFRs) into oxidized RAMs (i.e., quinoid C=O) via H<sub>2</sub>O<sub>2</sub> treatment. To our surprise, a slight decline in TCP oxidation (adsorptive removal was deducted) occurred for oBC400 at pH 3 (12.6%), 7 (9.3%), and 10 (19.3%), as compared to 26.0, 15.3, and 22.3% by BC400 (Figures 1a, S1d,e). Besides, the relative peak intensities of quinoid C=O experienced an increase after the TCP oxidation, as shown in FTIR spectra (Figure S14k) and XPS analysis (e.g., from 5.37 to 7.31 % for BC400, Figure S14f), suggesting that quinoid C=O might act as oxidized product, not reactants. Overall, these changes indicate the adverse effect of redundant quinoid C=O on PDS radical activation, as corroborated by the debilitated degradation performance of benzoic acid (i.e., a decreasing concentration of radicals in the oBC400/PDS system as compared to BC400, Figure S14m).

Furthermore, sodium borohydride was used to increase the phenolic –OH content of BC400. As expected, the content of phenolic –OH expanded from 0.16 to 0.30 mmol

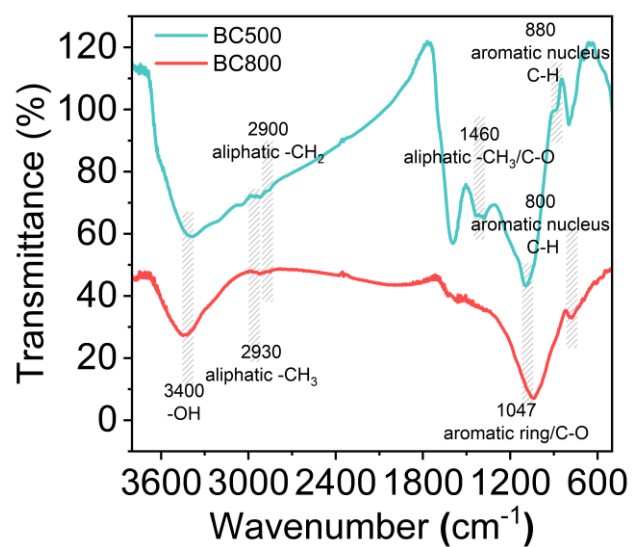
g<sup>-1</sup> (Table S8) and was accompanied by a diminution in both the amounts of quinoid C=O (from 4.3 × 10<sup>7</sup> groups g<sup>-1</sup> to 2.0 × 10<sup>7</sup> groups g<sup>-1</sup>, Table S8) and semiquinone-type PFRs (Figure S14l), meaning the successful reduction of RAMs. At pH 3, 28.4% of TCP was degraded by rBC400, higher than 26.0 % by BC400 (Figure 1a). Such an increased degradation efficacy also occurred under pH 7 (22.8%) and 10 (29.4%). These results indicated that the increasing phenolic –OH facilitated the TCP oxidation, which can be ascribed to the evolution of more radicals, as supported by the intensified removal of benzoic acid (Figure S14m). By releasing protons, phenolic –OH groups could be converted into organic radicals, which further induce the generation of SO<sub>4</sub><sup>•-</sup> (eq 10).<sup>37</sup>



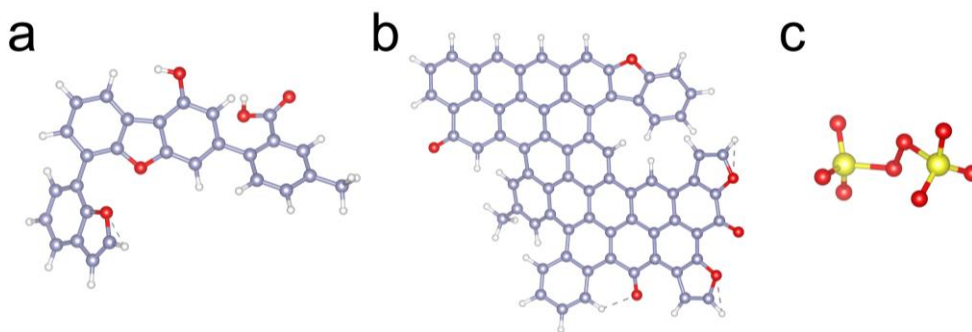
BC500 possessed less phenolic –OH but more PFRs (Table S8, Figure S14l), which demonstrated stronger catalytic capacity than BC400. To distinguish the role of PFRs, we then examined the changes in PFRs before and after the reactions. As shown in Figure S14n, the catalytic treatment substantially consumed the oxygen-centered PFRs intensity of BC500, while the adsorption of TCP alone had little effect on it. This indicates that PFRs might participate in the PDS activation and higher PFRs level favors TCP oxidation, which was reinforced by a poorer TCP degradation by used BC500 (after a catalytic experiment, 17.7%) than fresh BC500 (30.8%) as shown in Figure S14o. Also, Figures 1e and S4b depict the formation of the strongest radical (i.e., SO<sub>4</sub><sup>•-</sup>, <sup>•</sup>OH, and O<sub>2</sub><sup>•-</sup>) adduct signals in the BC500/PDS system, which further upheld the PDS radical activation triggered by PFRs. Possible pathways for radical generation included

587 1) PDS accepted electrons from PFRs to evolve  $\text{SO}_4^{\bullet-}$ ; 2) PFRs delivered electrons to  
588  $\text{O}_2$  to produce  $\text{O}_2^{\bullet-}$ , and then  $\text{O}_2^{\bullet-}$  reacted with PDS to produce  $\text{SO}_4^{\bullet-}$ ; 3)  $\text{SO}_4^{\bullet-}$  reacted  
589 with  $\text{H}_2\text{O}/\text{OH}^-$  to yield  $\cdot\text{OH}$ .

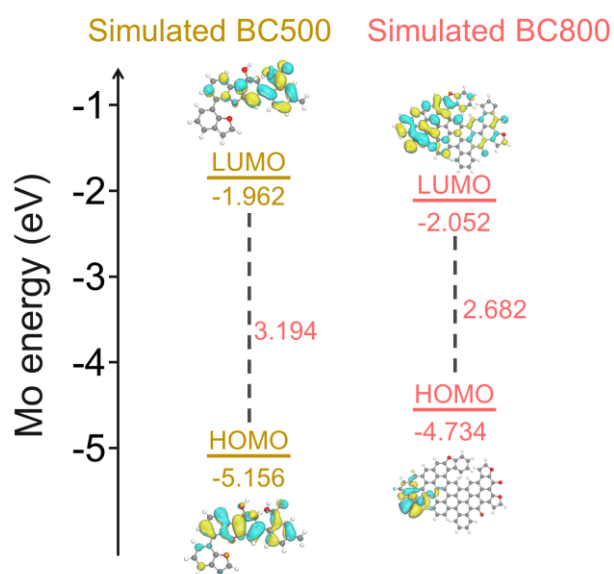




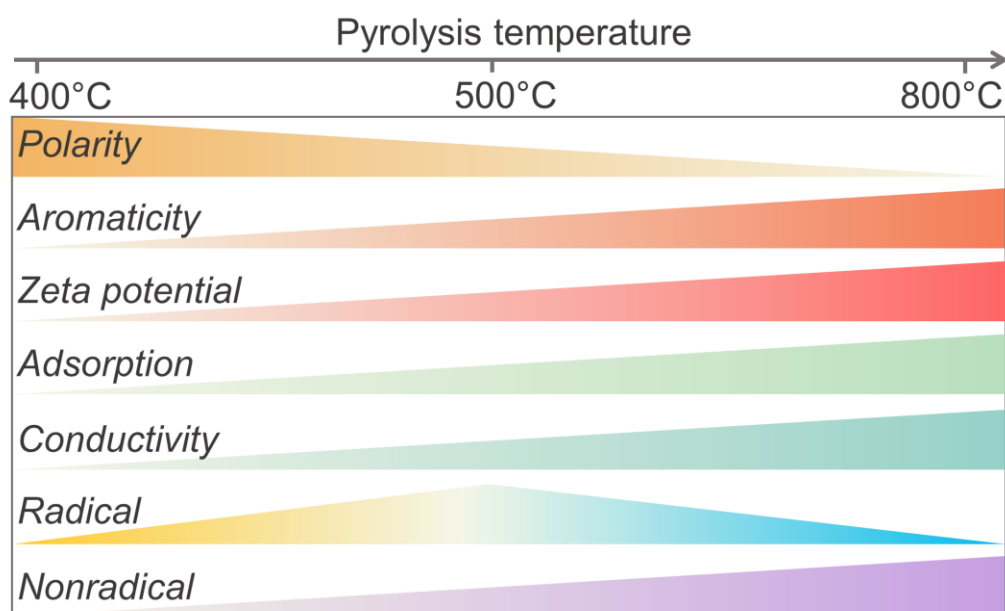
**Figure S15.** The FTIR spectrum of biochars.



**Figure S16.** Optimized configurations of BC500, BC800, and  $S_2O_8$ . (purple: C, white: H, red: O, yellow: S.)



**Figure S17.** Gaps between HOMO and LUMO of the biochar models.



**Figure S18.** Schematic diagram of biochar properties and reactivity as a function of pyrolysis temperature.

## References

- (1) Shao, P.; Jing, Y.; Duan, X.; Lin, H.; Yang, L.; Ren, W.; Deng, F.; Li, B.; Luo, X.; Wang, S. Revisiting the graphitized nanodiamond-mediated activation of peroxymonosulfate: Singlet oxygenation versus electron transfer. *Environmental Science & Technology* **2021**, 55 (23), 16078-16087.
- (2) Lei, Y.; Lu, J.; Zhu, M.; Xie, J.; Peng, S.; Zhu, C. Radical chemistry of diethyl phthalate oxidation via UV/peroxymonosulfate process: Roles of primary and secondary radicals. *Chemical Engineering Journal* **2020**, 379, 122339.
- (3) Xiao, X.; Chen, Z.; Chen, B. H/C atomic ratio as a smart linkage between pyrolytic temperatures, aromatic clusters and sorption properties of biochars derived from diverse precursory materials. *Scientific Reports* **2016**, 6 (1), 22644.
- (4) Chen, P.; Yang, R.; Pei, Y.; Yang, Y.; Cheng, J.; He, D.; Huang, Q.; Zhong, H.; Jin, F. Hydrothermal synthesis of similar mineral-sourced humic acid from food waste and the role of protein. *Science of the Total Environment* **2022**, 828, 154440.
- (5) Yan, J.; Lei, Z.; Li, Z.; Wang, Z.; Ren, S.; Kang, S.; Wang, X.; Shui, H. Molecular structure characterization of low-medium rank coals via XRD, solid state <sup>13</sup>C NMR and FTIR spectroscopy. *Fuel* **2020**, 268, 117038.
- (6) Kresse, G.; Furthmüller, J. Efficiency of ab-initio total energy calculations for metals and semiconductors using a plane-wave basis set. *Computational Materials Science* **1996**, 6 (1), 15-50.
- (7) Kresse, G.; Furthmüller, J. Efficient iterative schemes for ab initio total-energy calculations using a plane-wave basis set. *Physical Review B* **1996**, 54 (16), 11169-

- 630 11186.
- 631 (8) Perdew, J. P.; Burke, K.; Ernzerhof, M. Generalized gradient approximation made  
632 simple. *Physical Review Letters* **1996**, 77 (18), 3865-3868.
- 633 (9) Kresse, G.; Joubert, D. From ultrasoft pseudopotentials to the projector augmented-  
634 wave method. *Physical Review B* **1999**, 59 (3), 1758-1775.
- 635 (10) Blöchl, P. E. Projector augmented-wave method. *Physical Review B* **1994**, 50 (24),  
636 17953-17979.
- 637 (11) Kohn, W.; Sham, L. J. Self-consistent equations including exchange and  
638 correlation effects. *Physical Review* **1965**, 140 (4A), A1133-A1138.
- 639 (12) Marenich, A. V.; Cramer, C. J.; Truhlar, D. G. Universal solvation model based on  
640 solute electron density and on a continuum model of the solvent defined by the bulk  
641 dielectric constant and atomic surface tensions. *The Journal of Physical Chemistry B*  
642 **2009**, 113 (18), 6378-6396.
- 643 (13) *Gaussian 16, Revision C.01*; Gaussian, Inc, 2016.
- 644 (14) Humphrey, W.; Dalke, A.; Schulten, K. VMD: Visual molecular dynamics. *Journal*  
645 *of Molecular Graphics* **1996**, 14 (1), 33-38.
- 646 (15) Lu, T.; Chen, F. Multiwfn: A multifunctional wavefunction analyzer. *Journal of*  
647 *Computational Chemistry* **2012**, 33 (5), 580-592.
- 648 (16) Ren, W.; Xiong, L. L.; Yuan, X. H.; Yu, Z. W.; Zhang, H.; Duan, X. G.; Wang, S.  
649 B. Activation of peroxydisulfate on carbon nanotubes: Electron-transfer mechanism.  
650 *Environmental Science & Technology* **2019**, 53 (24), 14595-14603.
- 651 (17) Fan, X.; Lin, H.; Zhao, J.; Mao, Y.; Zhang, J.; Zhang, H. Activation of

652 peroxymonosulfate by sewage sludge biochar-based catalyst for efficient removal of  
 653 bisphenol A: Performance and mechanism. *Separation and Purification Technology*  
 654 **2021**, 272, 118909.

655 (18) Tan, W.; Ren, W.; Wang, C.; Fan, Y.; Deng, B.; Lin, H.; Zhang, H.  
 656 Peroxymonosulfate activated with waste battery-based Mn-Fe oxides for pollutant  
 657 removal: Electron transfer mechanism, selective oxidation and LFER analysis.  
 658 *Chemical Engineering Journal* **2020**, 394, 124864.

659 (19) Tian, W.; Lin, J.; Zhang, H.; Duan, X.; Wang, H.; Sun, H.; Wang, S. Kinetics and  
 660 mechanism of synergistic adsorption and persulfate activation by N-doped porous  
 661 carbon for antibiotics removals in single and binary solutions. *Journal of Hazardous*  
 662 *Materials* **2022**, 423, 127083.

663 (20) Qin, J.; Dai, L.; Shi, P.; Fan, J.; Min, Y.; Xu, Q. Rational design of efficient metal-  
 664 free catalysts for peroxymonosulfate activation: Selective degradation of organic  
 665 contaminants via a dual nonradical reaction pathway. *Journal of Hazardous Materials*  
 666 **2020**, 398, 122808.

667 (21) Zhao, C.; Zhong, S.; Li, C.; Zhou, H.; Zhang, S. Property and mechanism of phenol  
 668 degradation by biochar activated persulfate. *Journal of Materials Research and*  
 669 *Technology* **2020**, 9 (1), 601-609.

670 (22) Wu, Y.; Guo, J.; Han, Y.; Zhu, J.; Zhou, L.; Lan, Y. Insights into the mechanism of  
 671 persulfate activated by rice straw biochar for the degradation of aniline. *Chemosphere*  
 672 **2018**, 200, 373-379.

673 (23) Ma, W.; Wang, N.; Du, Y.; Tong, T.; Zhang, L.; Andrew Lin, K.-Y.; Han, X. One-

674 step synthesis of novel Fe<sub>3</sub>C@nitrogen-doped carbon nanotubes/graphene nanosheets  
 675 for catalytic degradation of Bisphenol A in the presence of peroxymonosulfate.  
 676 *Chemical Engineering Journal* **2019**, 356, 1022-1031.

677 (24) Cheng, X.; Guo, H.; Zhang, Y.; Wu, X.; Liu, Y. Non-photochemical production of  
 678 singlet oxygen via activation of persulfate by carbon nanotubes. *Water Research* **2017**,  
 679 113, 80-88.

680 (25) Olmez-Hanci, T.; Arslan-Alaton, I.; Genc, B. Bisphenol A treatment by the hot  
 681 persulfate process: Oxidation products and acute toxicity. *Journal of Hazardous*  
 682 *Materials* **2013**, 263, 283-290.

683 (26) Lin, Y.-T.; Liang, C.; Chen, J.-H. Feasibility study of ultraviolet activated  
 684 persulfate oxidation of phenol. *Chemosphere* **2011**, 82 (8), 1168-1172.

685 (27) Wojnárovits, L.; Takács, E. Rate constants of sulfate radical anion reactions with  
 686 organic molecules: A review. *Chemosphere* **2019**, 220, 1014-1032.

687 (28) Mei, Q.; Sun, J.; Han, D.; Wei, B.; An, Z.; Wang, X.; Xie, J.; Zhan, J.; He, M.  
 688 Sulfate and hydroxyl radicals-initiated degradation reaction on phenolic contaminants  
 689 in the aqueous phase: Mechanisms, kinetics and toxicity assessment. *Chemical*  
 690 *Engineering Journal* **2019**, 373, 668-676.

691 (29) Li, J.; Li, Q.; Steinberg, C. E. W.; Zhao, Q.; Pan, B.; Pignatello, J. J.; Xing, B.  
 692 Reaction of substituted phenols with lignin char: dual oxidative and reductive pathways  
 693 depending on substituents and conditions. *Environmental Science & Technology* **2020**,  
 694 54 (24), 15811-15820.

695 (30) Fendler, J. H.; Gasowski, G. L. Radiation-induced hydroxylation of nitrobenzene

696 in dilute aqueous solution. *Journal of Organic Chemistry* **1968**, 33 (5), 1865.

697 (31) Liang, C.; Su, H.-W. Identification of sulfate and hydroxyl radicals in thermally  
 698 activated persulfate. *Industrial & Engineering Chemistry Research* **2009**, 48 (11), 5558-  
 699 5562.

700 (32) Dorfman, L. M.; Harter, D. A.; Taub, I. A. Rate constants for reaction of hydroxyl  
 701 radical with aromatic molecules. *Journal of Chemical Physics* **1964**, 41 (9), 2954.

702 (33) Tratnyek, P. G.; Hoigne, J. Oxidation of substituted phenols in the environment: a  
 703 QSAR analysis of rate constants for reaction with singlet oxygen. *Environmental*  
 704 *Science & Technology* **1991**, 25 (9), 1596-1604.

705 (34) Al-Abduly, A. J.; Basfar, A. A.; Algamdi, M. S.; Alsohaimi, I. H.; Alharbi, A. A.;  
 706 Alkhedhair, A. M. Remediation and detoxification of water samples contaminated with  
 707 2, 4, 6-trichlorophenol by gamma radiation and ozonation. *Radiation Physics and*  
 708 *Chemistry* **2021**, 184, 109423.

709 (35) Wang, L.; Kong, D.; Ji, Y.; Lu, J.; Yin, X.; Zhou, Q. Formation of halogenated  
 710 disinfection byproducts during the degradation of chlorophenols by peroxymonosulfate  
 711 oxidation in the presence of bromide. *Chemical Engineering Journal* **2018**, 343, 235-  
 712 243.

713 (36) Fang, G.; Gao, J.; Liu, C.; Dionysiou, D. D.; Wang, Y.; Zhou, D. Key Role of  
 714 Persistent free radicals in hydrogen peroxide activation by biochar: Implications to  
 715 organic contaminant degradation. *Environmental Science & Technology* **2014**, 48 (3),  
 716 1902-1910.

717 (37) Yan, J.; Gao, W.; Dong, M.; Han, L.; Qian, L.; Nathanail, C. P.; Chen, M.

718 Degradation of trichloroethylene by activated persulfate using a reduced graphene  
719 oxide supported magnetite nanoparticle. *Chemical Engineering Journal* **2016**, 295,  
720 309-316.